IAC - 13.A6.1.7

Orbital Debris Parameter Estimation from Vertical Pointing Radar

Alan Li
Stanford University, USA, alanli@stanford.edu

Sigrid Close

Abstract

We present results from analysis of space debris data collected by the EISCAT radar at Svalbard. Approximately 90 hours of data were collected at the end of February 2008 after the Chinese anti-satellite (ASAT) test one year prior. Match function analysis is performed to obtain ranges, range rate and Signal-to-Noise Ratio (SNR) from the data set. We set the time interval between measurements to 0.08 seconds in order to match the short arc streaks to the symmetrical radar beam pattern; we then use these corrected data to produce the Radar Cross Section (RCS) of the debris. RCS gives the approximate sizes and mass estimates for the debris particles, which is combined with the measured altitude and velocity of the debris particles. Results are compared to NASA's collision model as well as Space-Track's catalogue of satellites. We show that even with the constraints of a vertically-pointing radar, a relatively unknown beam pattern and no tracking ability, we can still provide insightful analyses on space debris particles.

1. INTRODUCTION

From March 2007 to March 2009, the EISCAT Svalbard Radar (ESR) added its newly constructed space debris receiver to take measurements of orbital debris in addition to its typical ionospheric measurements [5]. Previous European Space Agency (ESA) studies, conducted between 2000 and 2005, demonstrated the feasibility of the EISCAT radar for debris detection using familiar transmission (but new data processing) techniques.

This paper extends the analysis on the Fenyun-1C meteorological spacecraft (International Designator 1999-025A, US satellite number 25730) presented at IAC 2012 [1]. The event involves the January 11th 2007 Chinese Anti-Satellite (ASAT) test, which the EISCAT Svalbard radar was able to detect beginning in February of the same year. The data here culminates in 4 days of almost uninterrupted observations beginning at 22:00 UT of February 18, 2008 through 22:00 UT of February 23, 2008.

The match function (MF) is used to detect the Doppler velocity and radar cross section (RCS) of detectable debris[1]. However a new algorithm was utilized to increase the resolution without changing the required computation time, which has led to new insight with the data. With this enhanced resolution, the SNR profiles can be calculated, and as such the symmetry point of these SNR profiles become important to the debris parameter calculations. Fitting range and range rate parameters to fairly circular orbits can also allow rough orbital characteristics to be inferred.

Comparisons will be made with Space-Track's Satellite Situation Report (SSR) and RCS data as well as NASA's collision model. AGI's Satellite ToolKit (STK) simulations are run in order to correlate our observations with Space-Track's Two Line Element (TLE) data. One important note is that although the ASAT test debris should comprise most of the debris observed, at the time of the observation the debris ring would have had ample time to become distributed. As such, not all observations made can be perfectly correlated to only Fenyun-1C debris.

2. DETECTION AND PARAMETER ESTIMATION

Parameter	Value
Transmission Frequency	499.85 MHz
Transmission Gain	43.9 dB
System Temperature	70 K
Elevation Angle	82.1°
Azimuth Angle	182.1°
Interpulse period (IPP)	3750 µs
Coherent Integration Time	0.24 sec

Table 1 EISCAT Radar Parameters

The EISCAT Svalbard radar (also known as Longyearbyen) is located at 78.2°N, 16°E and consists of 2 dishes (32m and 42m). Radar

parameters are described in Table 1. The radar beam crosses the debris ring twice per day, and because of the transmit-receive nature of the radar we have unobservable gaps in altitude. However for the sake of characterizing the ASAT debris, we will focus on the observable zone ranging from 700 to 1100 km.

Much of the techniques used are similar to that presented in [1], [3] and [4].

The Discrete Fourier Transform (DFT) version of the Match function,

$$MF(v, R_j) = \frac{\max\left[DFT\left(\langle z_n, \bar{x}_{n-j}\rangle\right)\right]}{\|x\|} \qquad [1]$$

is used to determine the range and range rate of the observed object. Here z is the received signal and $\bar{x}$ the complex conjugate of the transmitted signal, where these two inputs are element-wise multiplied to one another. We find the maximum of the DFT and normalize the result according to the magnitude of the transmitted signal. Depending on the amount that we shift the signal x relative to z (by index j), we will obtain different results, which is analogous to searching in the range space. The maximum of the DFT (for a particular index j) gives the range rate, and the maximum over the index j gives the range. The corresponding maximum range rate is then matched with the range at which the DFT is maximum. We increment the search by 0.1 seconds (approximately 26.7 IPP later) since the same piece of debris can usually be detected by the radar over this time interval. This gives an estimate on how the range rate and range changes over time. Figure 1 demonstrates this principle, with x_n and z_n the transmitted and received signals respectively.

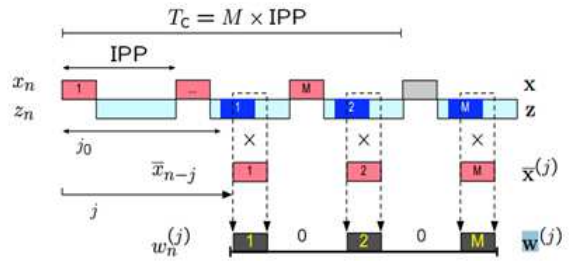

Figure 1. Depiction of transmit and receive signal, shifted by j and element-wise multiplied. The DFT is performed on ***w*** *afterwards and the maximum found.*

Ideally we would like to increment the index j by 1 every search to be as precise as possible, but this is computationally expensive. However, it is possible to allow this expensive procedure to be performed only at the first iteration in order to narrow down the index *j;* every subsequent search (i.e. every search 0.1 seconds before or after this initial point) is the performed around this initial index. We can therefore reduce the amount of computation time, but preserve our precision, resulting in a 1.25 m/s range rate resolution and 120 m range resolution. To yield the best results, the first search is initiated in the middle of the entire detection event so as to increase the likelihood of resulting in a high SNR near the beam center. If the first search does not yield a precise result, then it is likely subsequent searches will also be inaccurate. Figure 2 shows the results of this method, with the range, range rate, and SNR displayed over approximately 24 seconds.

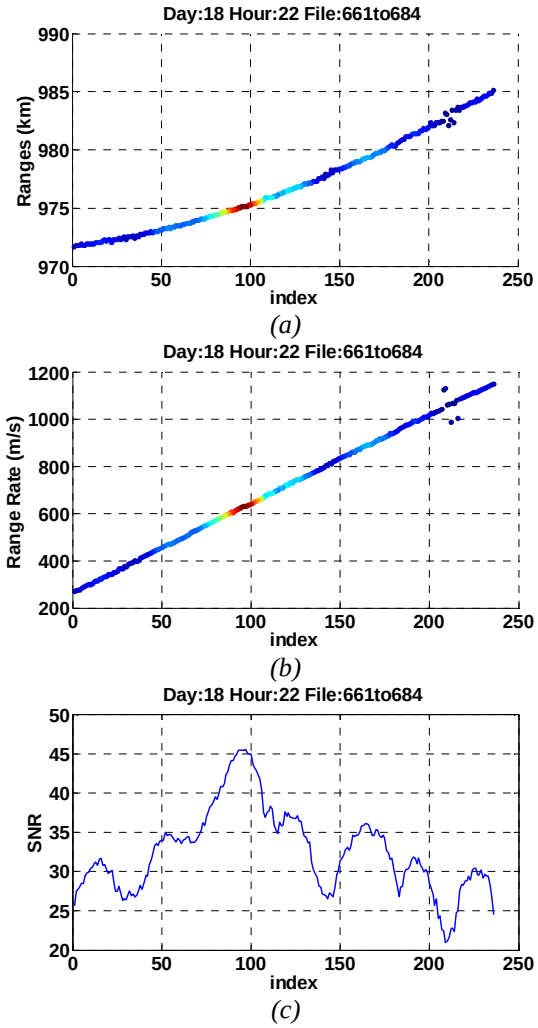

Figure 2. (a) Range data for a detection event. (b) Corresponding range rate data (c) Corresponding SNR profile

The Signal to Noise Ratio (SNR) is estimated as

$$\mathrm{SNR} \sim \frac{\max_{v,R} \mathrm{MF}^2}{\sigma_{\mathrm{noise}}{}^2} \qquad [2]$$

where *MF* is the Match Function, where the maximum is taken over *v*, velocity, and *R*, range. σ_{noise} is the standard deviation of the noise. The beam pattern thus becomes apparent as shown in Figure 2c. The RCS of the detected object is estimated as

$$RCS = \frac{(4\pi)^3 k_B T_{sys} R^4 SNR}{G(\phi)^2 \lambda^2 P_x D T_c} \qquad [3]$$

where k_B is the Boltzmann constant, T_{sys} the system temperature, *R* the range, *SNR* the signal to noise ratio, *G* the gain of the antenna, λ the wavelength, P_x the transmitted power, *D* the duty cycle, and T_c the coherent integration time.

The Raleigh approximation, assuming a spherically shaped object, gives an estimate on the diameter:

$$\frac{RCS}{\frac{1}{4}\pi d^2} = 9\left(\frac{\pi d}{\lambda}\right)^4 \qquad when\ d < \frac{\lambda}{\pi\sqrt{3}}$$
$$\frac{RCS}{\frac{1}{4}\pi d^2} = 1 \qquad when\ d > \frac{\lambda}{\pi\sqrt{3}} \qquad [4]$$

where *d* is the diameter of the object.

3. DATA

Performing the aforementioned data analysis on the entire 1.5 terabytes yields a series of positive detections over time. Because in this batch we used a modified DFT and SNR based search as opposed to that presented in [1] for initial detection trigger (a version of the previously mentioned DFT match function with larger time spacing and indices for searches), we hoped to reduce the number of noisy events present in the prior approach. The remainder of the noise was mitigated through active filtering.

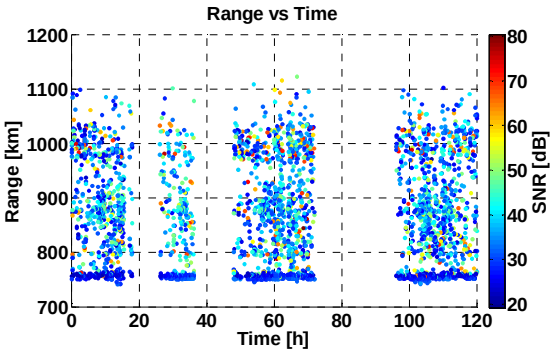

(a)

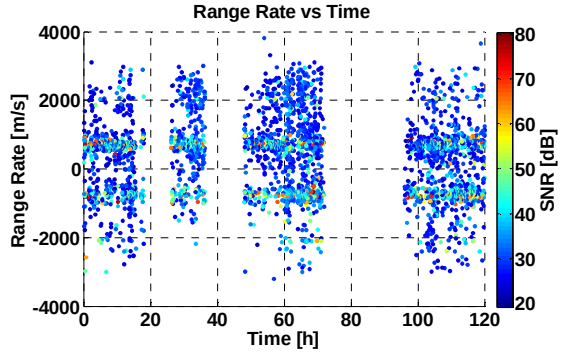

(b)

Figure 3. (a) Raw range vs. time data for detection events color-coded for SNR (b) Corresponding range rate vs. time data

In Figure 3, we see the resulting raw data, where the noise is apparent in the detection events occurring at approximately 750 km altitude due to radar ground clutter. However, we see distinct areas where there is an increase in the number of detection events, particularly between 850 and 1000 km altitudes. The range rate data also show most high SNR events (more likely to be debris events rather than simply noise) occur at ±700 m/s. The empty vertical regions are areas where the radar was not actively collecting debris data.

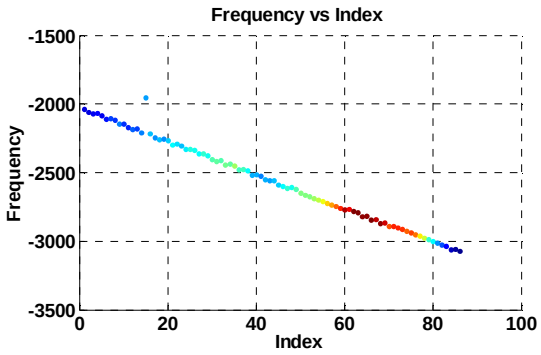

(a)

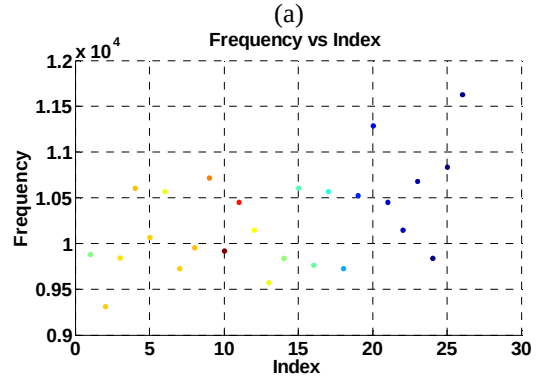

(b)

Figure 4 (a) A positive detection event (b) A noisy detection event, most likely due to radar ground clutter

The next step in our process to filter out the noise. The range rate data, in particular, is helpful in distinguishing signal from noise. As shown in Figure 4, detection events tend to have linear profiles in the range rate and parabolic profiles in the range data; we choose to analyze the range rate due to higher resolution and ease of linear fits. Noisy data will typically show no apparent profile and will tend to be very short in length (i.e. < 2 seconds in total duration). Given that a pure length filter allows for some noise events to be filtered into longer time scales, we combined a length filter with a linear filter. These results are shown in Figure 5. The data is filtered for detections longer than 2 seconds in length and a small coefficient of determination.

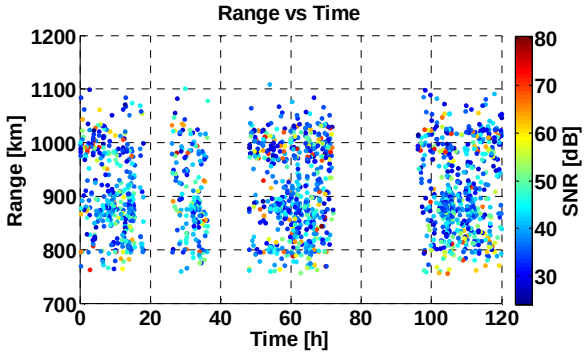

Figure 5.(a) Filtered range vs. time data for detection events color-coded for SNR (b) Corresponding filtered range rate vs. time data

As shown above, most of the noise seen in the 750 km range has been removed, and the range rate data is more focused towards the ±700 m/s region. Thus it seems that most of the noise also possess large and unreasonable Doppler rates.

Figure 6 shows two plots highlighting the characteristics of the filtered dataset. Figure 6a correlates the range and range rate, which are evenly split into two major velocity regions depending on if they are approaching the radar or travelling away from the radar. Figure 6b shows the range vs. length of detection; we see that we do get positive detections even for short duration events. The data also suggests that high SNR events tend to occur during longer detections, corresponding to larger objects being more easily detectable over a longer duration.

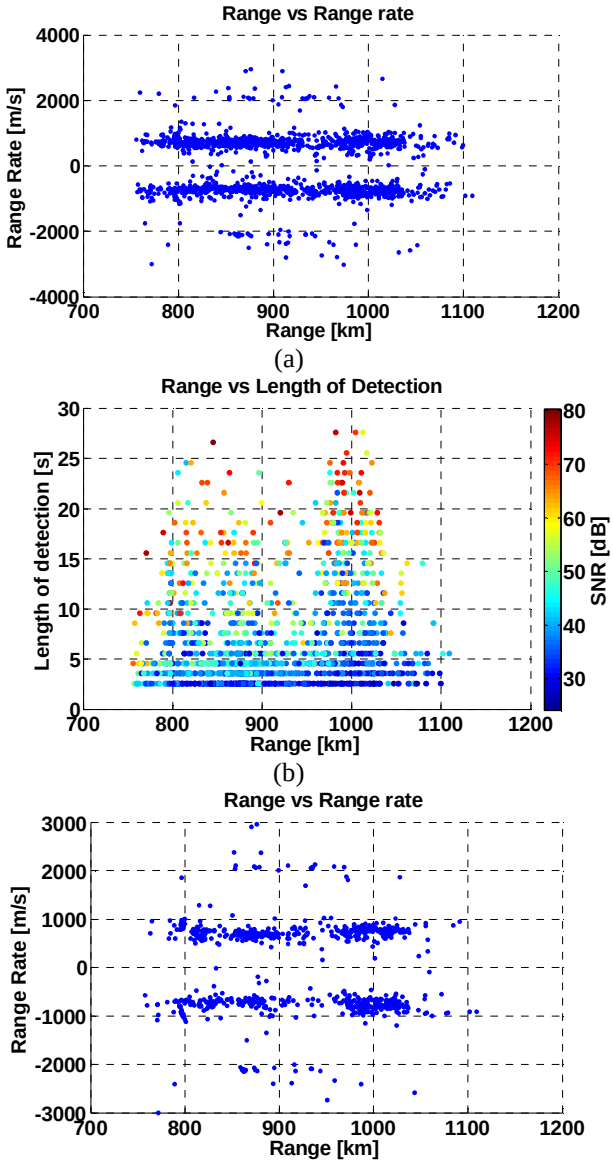

Figure 6. (a) Range vs. range rate, giving relative velocities for debris at different altitude for detection durations longer than 2 seconds (b) Range vs. duration of detection color-coded for SNR. (c) Range vs. range rate for detection durations longer than 5 seconds

If we make the assumption that larger pieces of debris correspond to larger SNRs and longer

durations, and filter the data by increasing the detection duration up to 5 seconds, we arrive at Figure 6c. Here we see that most of the larger detections are centered around 850 km (the altitude of the ASAT test) and near 1000 km.

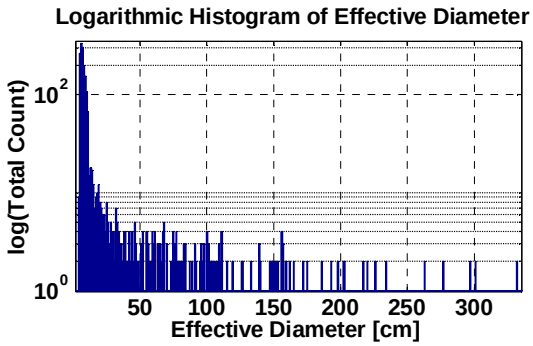

Figure 7 Logarithmic number of detection events for varying effective diameters

Using equations 3 and 4, we can arrive at effective diameters of the debris detected. We see a peak near 3 cm in diameter, hinting that most of the detections are indeed debris. There are very few detections with large diameters, and we see the characteristic tapering off of the number of debris at lower sizes due to radar sensitivity limitations.

4. ORBITAL PARAMETER ESTIMATION

It is difficult to determine orbital parameters, given the lack of an interferometric system. The problem is well known as the short arc problem, which attempts to estimate orbital characteristics from very short, but dense radar passes using the range and range rate data. However, we can impose a few assumptions that can allow us to determine the orbital characteristics in a generalized sense.

The first step is to fit the range and range rate data to parabolic and linear profiles, respectively using a 1 norm fit. It was found that a least squares fit tends to be skewed in terms of fitting due to the function attempting to minimize the distance to noisy measurements, while the 1 norm fit simply ignores these instances. The symmetry point of the SNR curve is then located, again using a 1 norm fit. This is a key point, since the location of importance is not the point of maximum SNR, but the point of symmetry. A piece of debris can conceivably pass through a null region of the radar beam pattern, and hence a symmetrical dip will be observed in the data (as shown in Figure 8a). If one searches around the area of maximum SNR, usually the point of symmetry can be found quite easily. However, there are instances where this might fail, if the debris goes directly through a null region of the beam pattern.

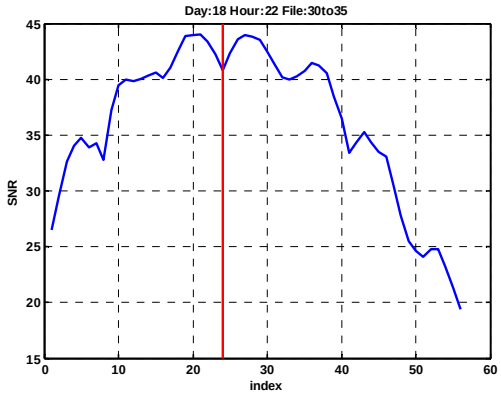

(a)

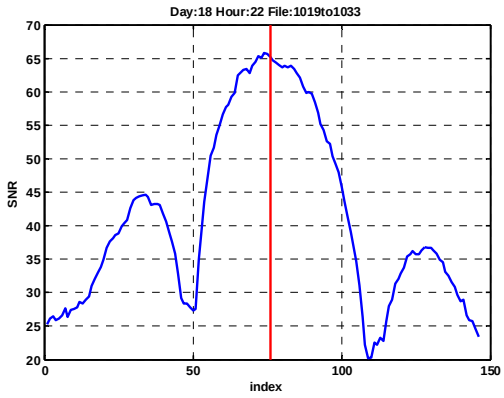

(b)

Figure 8 (a) Short duration detection event with symmetry point in a valley (b) Long duration detection event with clearly marked beam pattern

This location is then used in the calculation of the orbital characteristics. We use the estimated range and range rate from the previous fits at the location of symmetry of SNR to determine the approximate position and velocity of the debris according to

$$\vec{r}_{debris} = \vec{r}_{radar} + d_{est} * \overrightarrow{LOS} \qquad [5]$$

$$\|\vec{v}_{debris}\|\hat{v}_{debris} \cdot \widehat{LOS} = \dot{d}_{est} \qquad [6]$$

where $\vec{r}_{debris}$ is the position of the debris, $\vec{r}_{radar}$ the position of the radar site, d_{est} the estimated range of the debris as per the 1-norm fit, $\overrightarrow{LOS}$ the line of sight of the radar, $\dot{d}_{est}$ the estimated range rate of the debris as per the 1-norm fit, and $\vec{v}_{debris}$ the velocity. We can see that equation 5 gives a direct estimate on the object location, but equation 6 is slightly more subtle. Equation 6 implies that we do not in actuality

know the direction of the velocity vector, but only its magnitude when projected upon the line of sight vector. As such, if we then make an assumption on the direction of $\hat{v}_{debris}$, we can infer the magnitude of the velocity based upon the range rate information.

The idea is therefore to search through the directions that $\hat{v}_{debris}$ may take. To perform this, we first assume that $\hat{v}_{debris}$ is perpendicular to $\vec{r}_{debris}$, such that we define the object to be either at its apogee or perigee. We then rotate the vector an angle about $\vec{r}_{debris}$, and for every rotation we allow small angle adjustments of ±2° so that we remain roughly circular. This is akin to defining an azimuth and elevation for radar, and will term these angles θ and φ respectively. If we search through this space, we can propagate every orbit accordingly (assuming the debris passes through or roughly very close to the center of the radar beam) and construct the resulting range and range rate information.

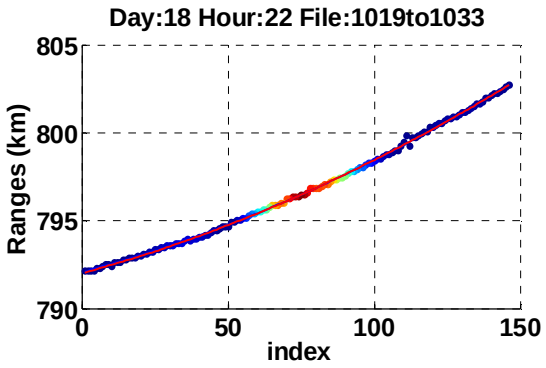

(a)

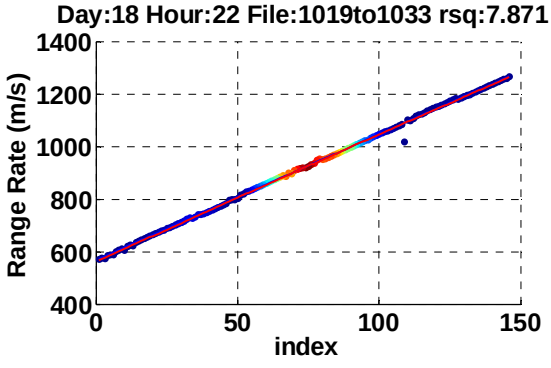

(b)

Figure 9 (a)Fit of range data for θ=15° and φ=0° for minimum eccentricity (b)Corresponding fit of range rate data for minimum eccentricity

Figure 9 displays the fits for minimum eccentricity to that of actual data. If we allow for all elliptical orbits, there would be an infinite number of orbits that would could be mapped onto the range and range rate information. However, limiting the eccentricity narrows down the search space and is a valid assumption for most debris. For long duration detections, the fits usually are quite decent (i.e. the fit in figure 9 has a normalized error of 7.871, which is defined as the sum of the absolute error divided by the number of points).

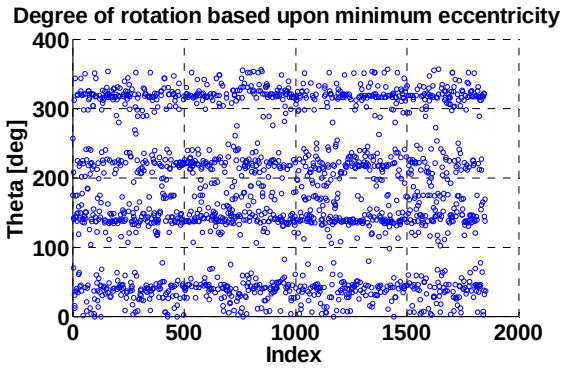

(a)

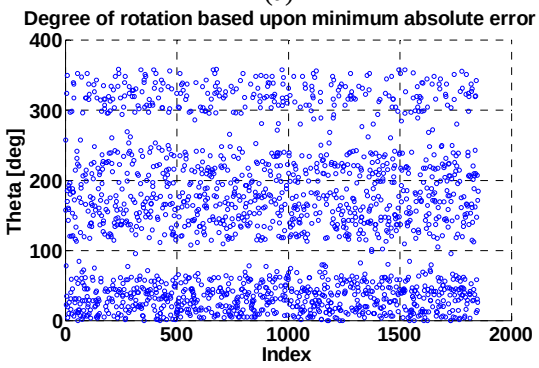

(b)

Figure 10 (a) θ rotation angle corresponding to minimum eccentricity (b) θ rotation angle corresponding to minimum absolute error

There are then two methods in which one may compare the propagated orbits to the dataset: either by minimum eccentricity or by minimum absolute error. Figure 10 shows the results of both of these methods; it is surprising to see that an assumption of minimum eccentricity forces the solution to aggregate into 4 distinct bands (Figure 10a), whereas the minimum absolute error gives results that follow no distinct pattern (Figure 10b). In actuality, each distinct band for the minimum eccentricity solution corresponds to a particular inclination, and since inclination values are only allowed up to 180°, there are then only two major inclination solutions. This is the unfortunate result of fitting these solutions, as they will always result in two fits that are identical but opposite in inclination by 90°. It is however unlikely that we see inclinations lower than 90° due to solar synchronous orbits at those altitudes, and hence can make the assumption that most inclinations

should be above 90°. Figure 11 shows the result of these assumptions, and the histogram of objects by inclination and eccentricity.

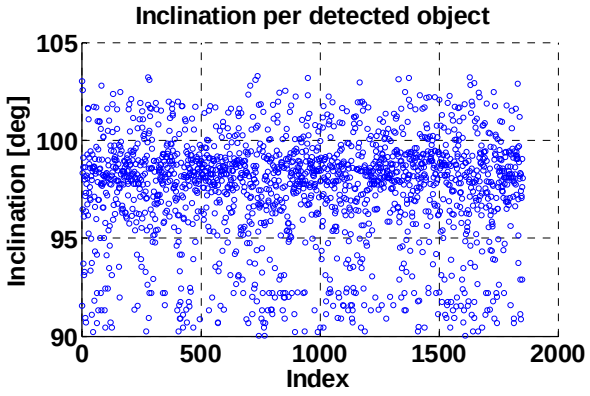

(a)

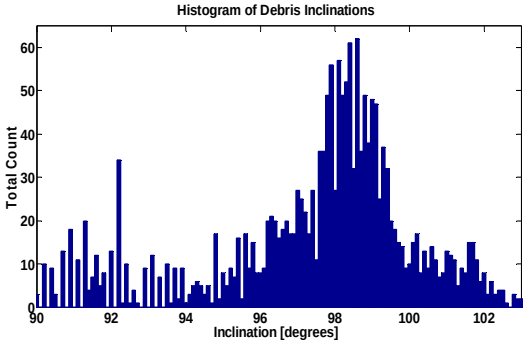

(b)

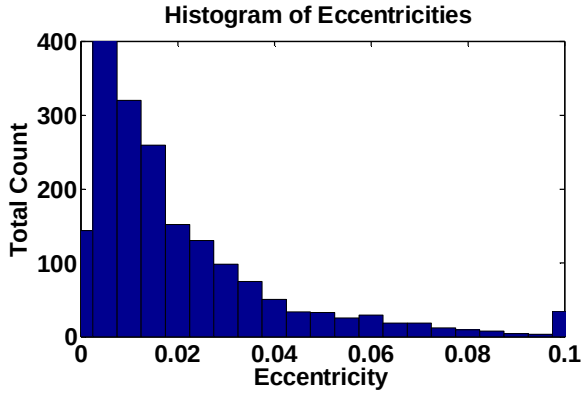

Figure 11(a) Inclination of detected objects for minimum eccentricity (b) Histogram of the same inclinations separated by 0.1° bins (c) Histogram of eccentricities per 0.005 value bins

The inclinations of the objects peak close to 99°. In part this is due to the number of solar synchronous orbits that exist at these altitudes, but it also reflects the sudden influx of debris from the ASAT test, which also has a peak number of objects at the same inclination. The eccentricities show that most orbits have a certain amount of eccentricity attached and are rarely perfectly circular.

5. DATA ANALYSIS AND COMPARISONS

Finally we compare the results to one another and to NASA and Space-Track data.

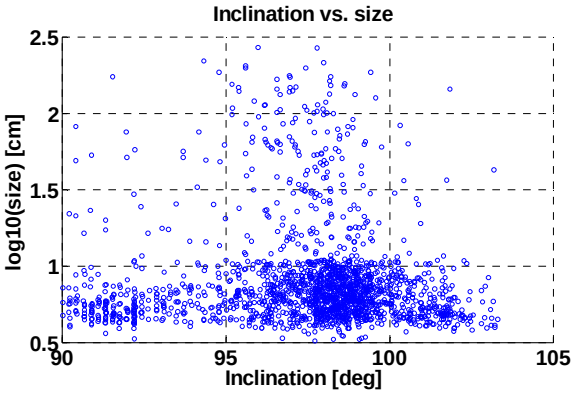

Figure 12 Inclination vs. size of debris. Note that the y axis is log10 of the diameter, where the diameter is in cm.

We examine the inclination vs. size of the debris detected as depicted by Figure 12. We see that most of the detections are within the single digit cm sizes, with the majority of detections at about 95° to 99°. As no major spacecraft at those altitudes are so small, it is most likely that most detections here is the result of the ASAT test (barring ionospheric scatter and range wrapping of the data).

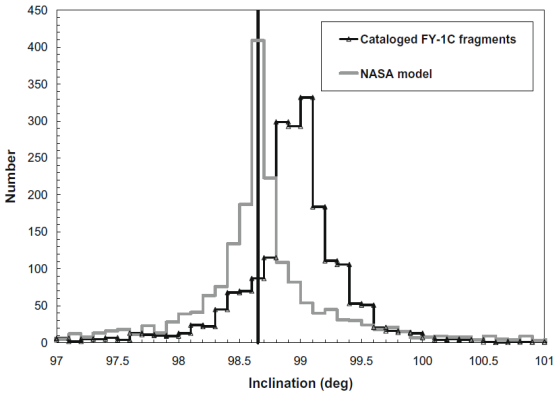

Figure 13 Inclination comparison between NASA model and catalogued fragments.

We now turn to the NASA collision model as seen in Figure 13. Here we see the actual inclinations of the ASAT debris, and comparing it with Figure 11b, we see peaks at similar inclinations. Figure 11b) is an estimate, and hence much of the best fits tend to leak into the adjacent inclinations.

Next we examine at the cumulative number of debris detected. We must be careful as to not to include the

entire dataset since some objects are not part of the ASAT event. We focus on the inclinations between 97° and 100° since most of the small RCS detections thought to be from the ASAT test reside in this region. Judging from Figure 13, we can see the marked shape of a collision similar to that of the NASA model. The data is skewed towards smaller pieces of debris since the gain used for the radar is the maximum gain (refer to equation 3), and hence decreases the RCS and therefore the estimated diameters. It has, however, been shown that EISCAT is able to detect well below the 10 cm threshold, which the NASA data does not display. This might also explain the marked increase in the number of smaller RCS detections. The comparisons are shown in Figure 14.

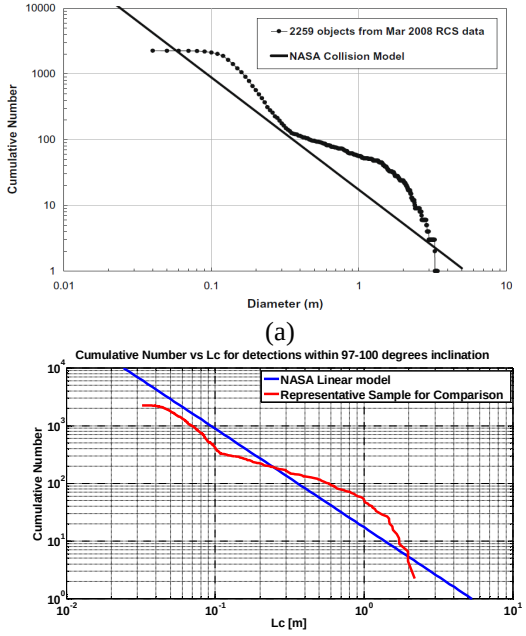

Figure 14 (a) Comparison between official SSR RCS data and NASA collision model. (b) Comparison between NASA collision model and EISCAT data filtered for inclinations between 97° and 100°. The red line normalizes the data to 2259 events in order to create a comparison between the official SSR RCS data.

We next run the TLEs from this same period through STK's deck access. This feature allows the user to specify the location and line of sight of the radar in conjunction with a half beam angle to determine when an object has passed through the radar beam. The deck access feature also displays the start and stop time of the detection and the range of the object.

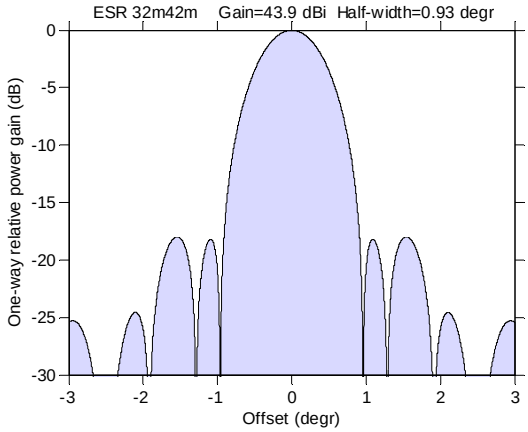

Figure 15 Theoretical beam pattern of radar

Figure 15 shows the theoretical beam pattern of the radar. We see major falloffs at ±1°, and the side lobes also disappear by ±2.5°. Running the deck access for the corresponding times for a 2.5° half angle yields 3564 detections. Lowering the half angle to 1.5° yields 1604 detections in our time and range criteria. Our total detection number before filtering stood at 3475 detections, although we removed what we perceived to be noisy and short duration events, resulting in 1737 detections. The EISCAT radar, using our filtering algorithm, is thus able to detect the as many debris as predicted by Space-Track data (if we assume a half angle of approximately 1.5°). Theoretically, it should be possible for EISCAT to possess more detection capability than that specified by the Space-Track catalogue, since it has been shown that it can be sensitive to objects less than 10 cm in diameter. As such, further analysis is required to determine a reasonable hit-miss ratio for the radar.

Moving forward with the 1.5° half angle since it corresponds best to the filtered dataset, we can then determine the number of detections that actually originate from the ASAT test. The TLE deck access yields 681 confirmed detections that were Fengyun debris, which brings the percentage of ASAT detections to 42.4%, meaning almost one half of all detections are debris. Moreover, we can see from Figure 16 the distinct bands that still correspond to the debris ring as well as a majority of the pieces in the 850 to 900 km range. Comparing this to Figure 5a, there is some similarity in the ranges but it is difficult to see the distinct bands with the excess noise and detection of other objects. Figure 16 shows the ASAT detections as predicted by STK's deck access tool over the same time period.

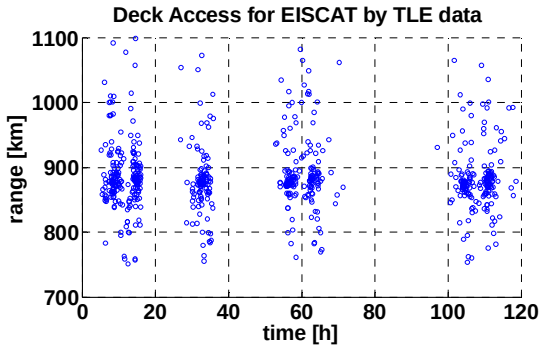

Figure 16 Fengyun detections as predicted by STK Deck Access tool. Dataset is modified to correspond to appropriate operation radar times and ranges.

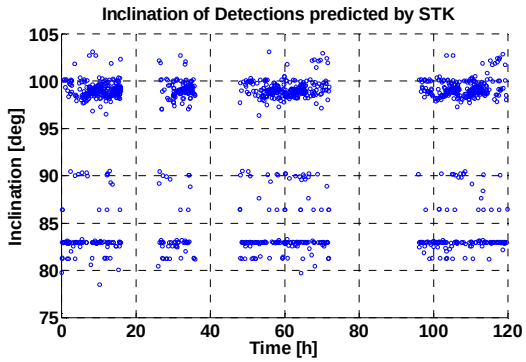

Figure 17 Inclination of Fengyun detections as predicted by STK Deck Access tool. Dataset is modified to correspond to appropriate operation radar times and ranges

We now make a final comparison regarding the inclinations from the historic TLE data. As seen in Figure 17, there lies a very distinct set of satellites at approximately 83°, but we can see that the debris at about 98° is much more chaotic due to the Fengyun incident. Using the inclinations from the TLEs, the percentage of objects with inclinations between 97° to 100° that is Fengyun debris stands at 64.5%. Thus more than half the debris detected at those inclinations are likely to be from the ASAT test.

6. CONCLUDING REMARKS

We have updated the methodology for debris detection by EISCAT using a method that searches the frequency space rigorously, and forcing subsequent searches about the region that yields the highest SNR. The first search is performed in the center of a particular detection event as to increase the likelihood of yielding a high SNR that corresponds to that particular detection. The method does not greatly increase the computation time but allows the greatest resolution possible with the radar.

The general orbital estimation problem from such short passes with only range and range rate data is very difficult, and usually two additional pieces of information is required to narrow down a specific orbit. However, we can make some general assumptions regarding the orbit: low eccentricity and high inclination. We can therefore best fit the orbit by varying the direction of the velocity vector. The result is that data tends towards the inclinations where the ASAT test occurred, reaffirming our assumptions.

Finally we compared the data to NASA models. The inclinations were spread out as compared to the official Space-track data, mainly due to errors in our best fit scenarios. The cumulative number result is actually quite similar to that reported previously (in [1]); the assumed large gain skews the results to smaller sizes.

The STK Deck Access tool was utilized to gain a perspective from the observables that should have resulted from historic TLEs. By adjusting the beam width angle by comparing theoretical and actual observed gain patterns, we arrived at a half angle of ±1.5°. The results show that roughly 42% of all detections, or roughly 65% of detections within the 97° to 100° inclination range are associated with the ASAT test. The inclination data also shows that the detections near the ASAT range is more chaotic than in other inclinations.

Our future work includes correlating specific STK Access events to radar events. In doing so, we will be able to directly assess the RCS differences across the two systems. This will allow the removal of the SNR beam pattern from the dataset, giving more precise and accurate estimates of the debris sizes. Long term goals include analyzing these SNR patterns to attempt to deduce shape patterns of the debris detected as well as tumbling rates.

7. REFERENCES

[1] Li, A., Close, S., Markannen, J. EISCAT Space Debris after the International Polar Year (IPY). Conference Proceedings from IAC 2012, 12.A6.1.8.

[2] Liou, J.-C., Johnson, N.L. Characterization of the Catalogued Fengyun-1C Fragments and their long-term effect on the LEO Environment. Advances in Space Research 43, 1407-1405.

[3] Markkanen, J., Lehtinene, M., Landgraf M. Real-time Space Debris Monitoring with EISCAT. Advances in Space Research 35, 1197-1208.

[4] Markkanen, J., Jehn, R., Krag, H. EISCAT space debris during the IPY – A 5000 hour campaign. 5th European Conference on Space Debris, March 2009.

[5] Markkanen J., Postila M. Real-time small-size space debris detection with EISCAT radar facilities, Final Report, ESOC Contract No. 16646/02/D/HK(CS), 2005. On-line as www.sgo.fi/~jussi/spade/FRII_21feb2005.pdf

[6] Markkanen J., Lehtinen M., Huuskonen A., Vaananen, A. Measurements of small-size debris with backscatter of radio Waves, Final Report, ESOC Contract No. 13945/99/D/CD, 2002. On-line as www.sgo.fi/~jussi/spade/FR_16Apr2002.pdf

[7] Anz-Meador, P.D., Matney, M.J. An Assessment of the NASA Explosion Fragmentation Model to 1 mm Characteristic Sizes. Advances in Space Research 34, 987-992.

[8] Johnson, N.L., Stansbery, E.G., Liou, J.-C., et al. The characteristics and consequences of the break-up of the Fengyun-1C spacecraft, Acta Astron., 21, 14, 2008.

[9] Johnson, N.L., Krisko, P.H., Liou, J.-C., Anz-Meador, P.D. NASA's new breakup model of evolve 4.0. Advances in Space Research 28, 1377-1384.

[10] Stansbery, G., Matney, M., Liou, J., Whitlock, D. A comparison of catastrophic on-orbit Collisions. Proceedings of the Advanced Maui Optical and Space Surveillance Technologies Conference, September 17-19, 2008. Ed.: S. Ryan, The Maui Economic Development Board, p.E50

[11] Kyle, T.A., Lewis, D. L.. Estimation of the Low Earth Orbit Space Object Population using a Non-Vertical Staring Radar. General Research Corp. Conference Proceedings from 1st European Space Debris Conference, 1993.

[12] Milania, A., Gronchi, G., Vitturi, M. and Knezevic, Z. Orbit Determination with Very Short Arcs. I Admissible Regions/ Celestial Mechanics and Dynamical Astronomy, Vol. 90, 2004, pp. 57-85.